Comparing the two amplitudes, we obtain

$$A = 1 - \frac{15\Sigma_e}{(11 + 6\nu - 5\nu^2)u_*^2} \tag{74}$$

from which a and $\tilde{a}_2$ follow again by Eqs. (44) and (54).

Hence, matching amplitudes in the hexagonal phase again leads to a linear relationship between A and Σ_e, but the prefactor differs compared with the plane-wave solution considered above.

However, irrespective of the chosen matching procedure, we obtain a linear relation between $\tilde{a}_2$ and $\tilde{c}$, leaving only one fitting parameter, $\tilde{c}$. Due to the linear dependence between $\tilde{a}_2$ and $\tilde{c}$ for both hexagonal and labyrinth patterns, one can use either matching relation to fit the experiments. Since the plane-wave (labyrinth) solution (67) leads to slightly simpler formulas, we choose the plane-wave matching in the following; that is, we assume that A and Σ_e are related by Eq. (69), and $\tilde{a}_2$ is given by Eq. (70). This convention means that we must determine $\tilde{c}$ by matching the theoretically predicted phase transition curve between the bistable and labyrinth states to the corresponding experimentally measured phase transition curve. The fitting value $\tilde{c}$ then automatically fixes the theoretical prediction for the second transition curve between hexagonal and bistable phase.

Phase diagram of the wrinkling morphology

The reduction of our effective theory to a standard Swift-Hohenberg equation allows us to make approximative predictions regarding the wrinkling morphologies. For the normal form, Eq. (65), three different wrinkling phases emerge depending on the choice of parameters A and B [14]:

$$\text{Unwrinkled:} \qquad 1 - A \leq 0 \tag{75a}$$

$$\text{Hexagons:} \qquad -\frac{1}{15}B^2 < 1 - A < \frac{4}{3}B^2 \tag{75b}$$

$$\text{Bistable phase:} \qquad \frac{4}{3}B^2 < 1 - A < \frac{16}{3}B^2 \tag{75c}$$

$$\text{Labyrinths:} \qquad \frac{16}{3}B^2 < 1 - A \tag{75d}$$

We recall that the coefficient B depends on κ via Γ_1, Γ_2, b and c, see Eq. (66), while A depends on the excess film stress and κ via Eq. (69). Substituting Eqs. (69) and (66) for A and B in Eq. (75), we obtain to leading order in κ the following stability criteria:

$$\text{Unwrinkled:} \qquad \Sigma_e \leq 0 \tag{76a}$$

$$\text{Hexagons:} \qquad -\frac{\rho}{20}\kappa^2 < \Sigma_e < \rho\kappa^2 \tag{76b}$$

$$\text{Bistable phase:} \qquad \rho\kappa^2 < \Sigma_e < 4\rho\kappa^2 \tag{76c}$$

$$\text{Labyrinths:} \qquad 4\rho\kappa^2 < \Sigma_e \tag{76d}$$

where

$$\rho = \frac{1}{\left[\eta^{1/3}(1-\nu)\tilde{c}\right]^2} \tag{76e}$$

The free parameter $\tilde{c}$ is a function of $\eta = 3E_s/E_f$ and ν. The functional form of $\tilde{c} = \tilde{c}(\eta, \nu)$ determines how the phase transition lines depend on those material properties. Comparison with our experimental data suggests, however, that the phase transition lines are in fact independent of η and ν (Fig. 3 of Main Text). In this case, ρ must be independent of η and ν, which means that

$$\tilde{c} = \frac{c_1}{(1-\nu)\eta^{1/3}}, \tag{77}$$

with fit parameter c_1. Adopting the ansatz (77), we find that $c_1 = 0.0188 \pm 0.0002$ gives the best fit to the experimental data (Fig. 3 of Main Text). The resulting good agreement with the data suggests strongly that the critical curves, which separate the different wrinkling phases in our experiments, are independent of material properties.

Hysteresis

We explain how the critical curves in Fig. 4 of Main Text are obtained. To this end, recall that the amplitude of the hexagonal solutions is given by Eq. (72). Inserting Eq. (69) for A gives

$$\mathcal{A} = \frac{2}{15}\left[Bu_* + \sqrt{(Bu_*)^2 + \frac{45\Sigma_e}{4}}\right] \tag{78}$$

To compare with the labyrinth solutions, we consider the measurable difference U_H of the maximal and minimal values of the hexagonal displacement field u_H (measured in units of h). Equation (71) implies that

$$U_\mathrm{H} = \max u_\mathrm{H} - \min u_\mathrm{H} = \frac{9}{2}\mathcal{A} \tag{79}$$

The prefactor in the last expression is due to the fact that u_H assumes its minimum at $-3\mathcal{A}$ and its maximum at $+3\mathcal{A}/2$.

To calculate the corresponding quantity U_L for the labyrinth solution u_L, we assume that labyrinths are locally described by the plane-wave $u_\mathrm{L} = \mathcal{A}\cos(k_c x)$. We then obtain with Eqs. (68) and (69)

$$U_\mathrm{L} = \max u_\mathrm{L} - \min u_\mathrm{L} = 2\sqrt{\Sigma_e} \tag{80}$$

Note that U_L is independent of curvature, whereas the square-root law for U_H is shifted horizontally and vertically by the Bu_*-terms (see Fig. 4b of Main Text). To first order in curvature, we have

$$Bu_* \simeq \frac{3\kappa}{4c_1} \tag{81}$$

DOI: 10.1038/NMAT4202

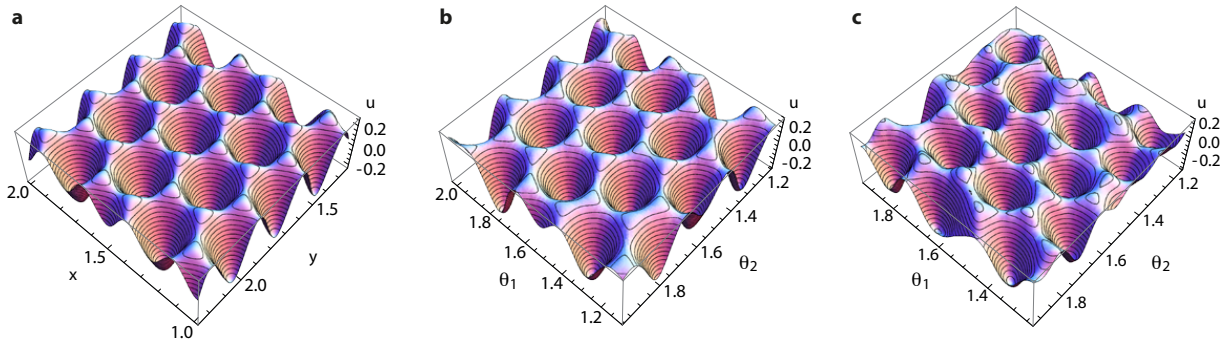

Fig. S1: Comparison of wrinkling morphologies in the hexagonal phase: (a) Planar analytical solution from Eq. (71), (b) numerical solution of the generalized Swift-Hohenberg theory from Eq. (43) (simulation parameters: $\gamma_0 = -0.08$, $a = 0.0151$, $c = 0.0095$, $R/h = 80$), and (c) 3D surface scan from experiments ($R = 20$mm, $h = 0.375$mm, $E_f = 2100$kPa, $E_s = 230$kPa). θ_1 and θ_2 denote polar angles.

yielding for the horizontal and vertical shifts (see Fig. 4b in the Main Text)

$$\delta\Sigma_e = \frac{\kappa^2}{20c_1^2}, \qquad \delta U_{\mathrm{H}} = \frac{9\kappa}{10c_1} \tag{82}$$

Based on the results for U_{L} and U_{H}, we expect two hysteresis cycles (see Fig. 4 of Main Text). The first cycle is due to the shift $\delta\Sigma_e$, which creates a subcritical stability zone for the hexagonal solutions [14]. Increasing Σ_e from the unwrinkled phase, hexagons emerge at the onset $\Sigma_e = 0$. However, once they have formed, hexagons remain stable even if the excess stress Σ_e is subsequently reduced below the wrinkling onset $\Sigma_e = 0$. Only for $\Sigma_e < -\delta\Sigma_e$, hexagons loose stability and the unwrinkled solution remains as the only stable state. The second hysteresis cycle involves larger excess stresses (see Fig. 4a of Main Text). Starting from the hexagonal phase, hexagons remain stable if the excess stress is increased into the bistable phase [14]. Only if Σ_e is increased beyond the bistable-to-labyrinth transition line, hexagons loose their stability and the system jumps to a labyrinth state. Upon decreasing Σ_e from the labyrinth phase, the system adopts a different path as labyrinths remain stable throughout the bistable phase; a transition to hexagons happens when Σ_e is decreased below the critical value that separates the hexagonal from the bistable phase.

Validation of hexagonal patterns

To test our effective theory further, we compare the planar hexagon solution, Eq. (71), with the numerical solution of Eq. (43) on a spherical geometry (Fig. S1a,b). The good agreement between analytical and numerical solution confirms that the effective theory is indeed well approximated by the standard planar SH equation (65). These results corroborate that once hexagons are selected, curvature has negligible influence on their morphology. Moreover, analytical and numerical solutions compare well with the experimentally determined 3D surface scans (Fig. S1c), demonstrating that the presented effective theory is able to reproduce the morphological details of thin film buckling patterns.

TOROIDAL GEOMETRIES

We consider a torus with major radius R_1 and minor radius R_2 measured in units of h. Using Eq. (1) and the standard surface parametrization $\mathbf{S} = [(R_1 + R_2\cos\theta_2)\cos\theta_1, (R_1 + R_2\cos\theta_2)\sin\theta_1, R_2\sin\theta_2]$ with coordinates $(\theta_1, \theta_2) \in [0, 2\pi) \times [0, 2\pi)$ we obtain the metric tensor

$$(a_{\alpha\beta}) = \begin{pmatrix} (R_1 + R_2\cos\theta_2)^2 & 0 \\ 0 & R_2^2 \end{pmatrix} \tag{83}$$

Equation (5a) yields for the curvature tensor

$$(b_{\alpha\beta}) = \begin{pmatrix} -\cos\theta_2(R_1 + R_2\cos\theta_2) & 0 \\ 0 & -R_2 \end{pmatrix} \tag{84}$$

and, from Eq. (26), one finds mean and Gaussian curvature as

$$\mathcal{H} = -\frac{1}{2}\left(\frac{\cos\theta_2}{R_1 + R_2\cos\theta_2} + \frac{1}{R_2}\right) \tag{85a}$$

$$\mathcal{K} = \frac{\cos\theta_2}{R_1 R_2 + R_2^2\cos\theta_2} \tag{85b}$$

Recall that the coefficients $\tilde{a}$, $\bar{\gamma}$, and $\tilde{a}_2$ were determined in the previous section using asymptotic comparison with the flat case. Hence, the expressions for these coefficients remain valid for toroidal geometries. Moreover, we observe that only the symmetry-breaking term in Eq. (34) contains contractions of the curvature tensor of first order, whereas the coefficients (33c) only depend on curvature at second or higher order. For instance, for

Fig. S 2: Wrinkling morphologies on a toroidal geometry with $R_1 = 80$ and $R_2 = 16$ for increasing excess film stress: (a) $\Sigma_e = 0.25$, (b) $\Sigma_e = 0.5$ and (c) $\Sigma_e = 2.0$. As in spherical geometries, one observes a transition from hexagonal to labyrinth-like patterns with increasing excess stress Σ_e. However, in contrast to the spherical case, the non-constant curvature on the torus can lead to local symmetry-breaking, i.e., at intermediate values of Σ_e labyrinth patterns are more likely to emerge at the inner saddle-like regions of the torus, see (b), whereas hexagons remain stable in the outer regions of the torus, where the two principal curvatures have the same sign resulting in a larger mean curvature. Simulation parameters are $\gamma_0 = -0.079$, $c = 0.075$, (a) $a = 0.017$, (b) $a = 0.016$, and (c) $a = 0.007$, using an unstructured surface triangulation with $> 26,000$ nodes.

a toroidal geometry with $R_1 = 80$, $R_2 = 16$, and $\eta = 0.33$ as shown in Fig. S2, we have $\gamma_0 = -0.079$, so that $|\gamma_0|$ is much larger than the maximum curvature correction $\max_{\theta_1,\theta_2} |\mathcal{R}/6| \approx 0.0007$. We can therefore neglect curvature corrections in the coefficients (33c).

Simulations of Eq. (34) confirm that a symmetry-breaking transition from hexagonal to labyrinth-like structures can also be observed on toroidal geometries when the excess stress is increased (Fig. S2). However, as curvature is now spatially varying, we find that the transition occurs first in the inner regions of the torus, where the principle curvatures have opposite sign (Fig. S2b). In the outside regions, where both principal components have the same sign, hexagons remain stable for relatively larger overstresses, until they become also unstable eventually (Fig. S2c).

In summary, Fig. S2 illustrates that the generalized theory derived above can be applied to arbitrarily curved surfaces.

[1] P. G. Ciarlet. *Mathematical elasticity, vol. III: Theory of shells*. North Holland, 2000.
[2] D. Breid and A. J. Crosby. Curvature-controlled wrinkle morphologies. *Soft Matter*, 9:3624–3630, 2013.
[3] M. M. Müller, M. Deserno, and J. Guven. Interface-mediated interactions between particles: A geometrical approach. *Phys. Rev. E*, 72(6):061407, 2005.
[4] W. Helfrich. Elastic properties of lipid bilayers: theory and possible experiments. *Z. Naturforsch.*, 28(11):693–703, 1973.
[5] Z. Y. Huang, W. Hong, and Z. Suo. Nonlinear analyses of wrinkles in a film bonded to a compliant substrate. *J. Mech. Phys. Solids*, 53:2101–2118, 2005.
[6] J. Swift and P. C. Hohenberg. Hydrodynamic fluctuations at the convective instability. *Phys. Rev. A*, 15(1):319–328, 1977.
[7] M. C. Cross and P. C. Hohenberg. Pattern formation outside of equilibrium. *Rev. Mod. Phys.*, 65(3):851–1112, 1993.
[8] H. G. Allen. *Analysis and Design of Structural Sandwich Panels*. Pergamon, New York, 1969.
[9] S. Cai, D. Breid, A. J. Crosby, Z. Suo, and J. W. Hutchinson. Periodic patterns and energy states of buckled films on compliant substrates. *J. Mech. Phys. Solids*, 59:1094–1114, 2011.
[10] L. D. Landau and E. M. Lifshitz. *Elasticity theory*. Pergamon Press, New York, 1975.
[11] Y. Jeong, Y.-C. Chen, M. K. Turksoy, S. Rana, G. Y. Tonga, B. Creran, A. Sanyal, A. J. Crosby, and V. M. Rotello. Tunable elastic modulus of nanoparticle monolayer films by host–guest chemistry. *Advanced Materials*, in press, doi: 10.1002/adma.201401226, 2014.
[12] G. Cao, X. Chen, C. Li, A. Ji, and Z. Cao. Self-assembled triangular and labyrinth buckling patterns of thin films on spherical substrates. *Phys. Rev. Lett.*, 100(3):036102, 2008.
[13] J. Yin, Z. Cao, C. Li, I. Sheinman, and X. Chen. Stress-driven buckling patterns in spheroidal core/shell structures. *Proc. Natl Acad. Sci.*, 105(49):19132–19135, 2008.
[14] A. A. Golovin and A. A. Nepomnyashchy. *Self-assembly, pattern formation and growth phenomena in nano-systems*. Springer, Dordrecht, 2006.